



PCCP

**Dynamic interplay between interfacial nanobubbles:
Oversaturation promotes anisotropic depinning and bubble
coalescence**

Journal:	<i>Physical Chemistry Chemical Physics</i>
Manuscript ID	CP-ART-07-2021-003451.R1
Article Type:	Paper
Date Submitted by the Author:	24-Sep-2021
Complete List of Authors:	Nag, Sarthak; Kyushu University, Mechanical Engineering Tomo, Yoko; Kyushu University, Mechanical Engineering Teshima, Hideaki; Kyushu University, Aeronautics and Astronautics Takahashi, Koji; Kyushu University, Aeronautics and Astronautics Kohno, Masamichi ; Kyushu University,

SCHOLARONE™
Manuscripts

ARTICLE

Dynamic interplay between interfacial nanobubbles: Oversaturation promotes anisotropic depinning and bubble coalescence†

Received 00th January 20xx,
Accepted 00th January 20xx

DOI: 10.1039/x0xx00000x

Sarthak Nag,^{‡ab} Yoko Tomo,^{‡a} Hideaki Teshima,^{bc} Koji Takahashi,^{bc} Masamichi Kohno^{*ab}

Probing the nanobubbles' dynamics is essential to understand their longevity and behavior. Importantly, such observation requires tools and techniques having high temporal resolutions to capture nanobubble's intrinsic characteristics. In this work, we have used the in-situ liquid-phase electron microscopy technique (LPEM) to gain insights into nanobubbles' behavior and their interfacial dynamics. Interestingly, we could observe a freely growing-shrinking nanobubble and a pinned nanobubble at the same experimental conditions, suggesting the possibility of multiple nanobubble stabilization theories and pathways. Remarkably, the study reveals that a freely growing-shrinking nanobubble induces anisotropic depinning in the three-phase contact line of a strongly pinned neighboring nanobubble. The anisotropic depinning is attributed to the differential local gas saturation levels, depending on the relative positioning of freely growing-shrinking nanobubble. Further, we also observed the unique pull-push phenomenon exhibited by the nanobubble's interfaces, which is attributed to the van der Waals interactions and the electric double layer, collectively. The role of the electric double layer in suppressing and delaying the merging is also highlighted in this study. The present work aims to reveal the role of locally varying gas saturation in the depinning of nanobubbles, their longevity due to electric double layer, and the consequent coalescence, which is crucial to understand the behavior of nanobubbles. Our findings will essentially contribute towards the understanding of these novel nanoscale gaseous domains and their dynamics.

Introduction

The progression from macroscales to nanoscales, especially at the interfaces, induces notorious behaviors and much-unexpected transition from the familiar bulk behavior.^{1,2} On a similar tone, surface nanobubbles^{3–6} have continued to perplex researchers for nearly three decades now.⁷ The classical Young-Laplace equation, otherwise valid at the nanoscale,⁸ predicts an unusual high internal pressure of tens of atmospheres inside a bubble of a few nanometer radius. Likewise, the Epstein-Plesset theory on the stability and dynamics of gas bubbles⁹ predicts the dissolution timescales in the range of few microseconds for nanobubbles,^{10,11} yet their week-long stability has been confirmed using numerous experimental techniques.^{12,13} Therefore, efforts are required to investigate their dynamic behavior. In addition, their unique applications and the functional advantages, for instance, in chemical energy

storage,¹⁴ surface cleaning,¹⁵ water treatment,¹⁶ assisted nanofabrication,¹⁷ boiling nucleation,¹⁸ and surface drag reduction¹⁹ have thrust the interest to understand their behavior and dynamics to further explore their potential applications.

Numerous experimental techniques have been applied to demonstrate the existence of surface nanobubbles and to characterize their behavior:⁵ atomic force microscopy (AFM),^{20–25} optical microscopy,^{26–28} scanning transmission X-ray microscopy (STXM),^{29,30} and liquid-phase electron microscopy (LPEM).^{31–35} AFM has been used extensively due to its capability of providing information about the three-dimensional topography of nanobubbles and studying characteristics like contact angles, height and longevity as well as distinguishing between the nanobubbles and micro/nano-pancakes.^{36,37} In fact, the long-term stability of surface nanobubbles has been proved experimentally using AFM. However, the time resolution of AFM is in order of tens or hundreds of seconds which renders them unsuitable to capture the dynamic behavior of nanobubbles. Advanced optical microscopy techniques have good temporal resolutions to capture nanobubbles' dynamic behavior but are incapable to capture ultra-fine nanobubbles having a size less than 100 nm.²⁷ Similarly, STXM also has a low spatio-temporal resolution, although it provides comprehensive information about the density of the gas phase in and around nanobubbles which contributes towards the understanding of gas behavior at the nanoscale.^{29,30} LPEM, on the other hand, can observe the

^a Department of Mechanical Engineering, Kyushu University, Fukuoka 819-0395, Japan. E-mail: kohno@mech.kyushu-u.ac.jp

^b International Institute for Carbon-Neutral Energy Research (WPI-I2CNER), Kyushu University, Fukuoka 819-0395, Japan.

^c Department of Aeronautics and Astronautics, Kyushu University, Fukuoka 819-0395, Japan.

[‡] Equal authorship.

[†] Electronic Supplementary Information (ESI) available: Movie of the observed phenomenon; water drop contact angle on SiNx e-chips; time history of observed nanobubbles; interaction between bubbles on adjacent windows; similar phenomenon observed in other nanobubble pairs; long-term variations in the nanobubble pair. See DOI: 10.1039/x0xx00000x

nanobubbles with high temporal and spatial resolutions.^{34,38} Moreover, the in-situ nanobubble nucleation in the protic liquids due to radiolysis mediates the high time-resolved observation of the bubble dynamics such as their growth, shrinking, and dependence on the neighboring nanobubbles which holds importance in characterizing these nanoscale domains. Recent investigations on nanobubbles using transmission electron microscopes (TEM) have unveiled distinctive nanoscale gas transport and nanobubble behavior, such as direct fast gas transport between the nanobubbles through the instantaneous rupture of the ultrathin liquid film in a graphene liquid cell.³⁹ A similar study using graphene liquid cell revealed the dependence of inter-bubble gas transport, bubble shape, and bubble growth on the relative size of the nanobubbles.⁴⁰ Additionally, the advancements in nanofabrication and the development of silicon nitride (SiN_x) membrane liquid cells have helped in understanding nanobubble dynamics with better control over nucleation surfaces, liquid thickness, and other physical parameters. SiN_x cell based LPEM has revealed significant gas and nanobubble behavior at nanoscale such as the diffusive shielding for smaller nanobubbles,³² unexpected homogenous nucleation of nanobubbles near the solid-liquid interface³³ and more recently, the mechanistic involved in pinned surface nanobubble merging.³⁵ Hence, the application of LPEM in observing and understanding nanobubble dynamics becomes highly relevant.

The available literature attributes the stability of the surface nanobubbles to the oversaturation and contact line pinning.^{41–43} However, nanobubbles exhibit complex phenomena and it is difficult to construe the stability of nanobubbles on basis of any single novel model. Additionally, nanobubbles have been observed to be stable, both numerically and experimentally, in normal, or even in undersaturated conditions rather than undergoing dissolution.^{44–46} On the contrary, the stability of the surface nanobubbles, in absence of contact line pinning, has also been studied and seems valid.^{47,48} Hence, understanding the nanobubbles' phenomenon and dynamics is tedious and requires further studies to answer such complex physiochemical phenomena. LPEM, due to its high temporal resolution, has revealed the shrinking, growing, and merging of nanobubbles in real-time,^{33,39,49} which also advocates for its utilization to understand the phenomenon that can provide answers towards stability and longevity of nanobubbles. On the other hand, several literatures also contemplate the role of the diffused double layer in the existence and stabilization of nanobubbles.^{4,50–54} The charges at the bubble interface and their repulsive interaction create a net electrostatic pressure acting radially outwards, opposite to the Laplace pressure. An individual nanobubble is, therefore, encompassed in its electric double layer whose thickness is a function of ionic concentration, liquid properties, and temperature.⁵⁵

In the present investigation, we have used LPEM to focus on the interactions between surface nanobubbles. The salient feature of this study is that we could observe nanobubbles with radii less than 50 nm at a higher resolution for a long duration, which allowed us to understand the slow-interplay these bubbles

undergo. The nanobubbles were nucleated and probed in thin water film using the TEM. We observed neighboring nanobubbles showing contrasting behavior at similar experimental conditions: pinned nanobubble and freely growing-shrinking nanobubble. Next, we studied the interactions among the contrasting nanobubbles and found that the shrinking of the unpinned nanobubbles induces directional depinning in the pinned nanobubbles. This signifies the anisotropic gas transport as well as the presence of localized saturation regions near the interface. Further, the push-pull phenomena between the bubble interfaces were observed multiple times. We consider that the electric double layer exhibiting repulsive interaction is responsible for the push, whereas the attractive van der Waals interaction, coupled with the localized high saturation regions is responsible for the pull or the directional depinning. Last, we propose and evaluate the interacting pathway for these nanobubbles. Along with highlighting the utility of LPEM in understanding nanobubbles, the presented work essentially demonstrates the interplay between the nanobubbles, along with evaluating the stability of nanobubbles and gas transport at the nanoscale.

Experimental Methods

We used an in-situ electron microscopy system (Poseidon Select, Protochips Inc., U.S.A.) for the direct visualization of fluids in the TEM. Figure 1A shows the schematic representation of the liquid cell. The details of the experimental equipment and procedures have been described elsewhere,³⁵ however briefly, a water film was encapsulated between the silicon e-chips having 50 nm thick suspended SiN_x windows of dimensions 550 μm × 50 μm, and spacer gap of 150 nm. The surface of these silicon e-chips was cleaned and hydrophilized using a glow discharge plasma reactor (PIB-10, Vacuum Devices, Japan). This is an important step to encapsulate a stable water film at such nanoconfinement levels and avoid liquid film retractions. This also rendered high hydrophilicity to the SiN_x chip with static contact angle <5°, as shown in the ESI† (Figure S1). Water used in the experiments was purified and deionized using a reverse osmosis water purifier (Aquarius RFP742HA, Advantec, Japan). Although deionized water was used for the experiment, carbon dioxide from the atmosphere is expected to increase the pH of the water due to the absorption of carbon dioxide. Hence, the initial ionic strength and the pH of the water were 2 × 10⁻⁶ M and 5.6, respectively. After the assembly of the in-situ electron microscopy system, it was placed in the vacuum station and the water was continuously flowed to check for leaks and avoid drying. It is important to note that the central region of the SiN_x windows of the liquid cell undergoes massive bowing due to the high vacuum in the TEM column, as depicted in Figure 1A, and the liquid thickness is generally much larger than the spacer height.

TEM (JEM-2100Plus Electron Microscope, JEOL Ltd., Japan), operating at 200 kV, was used to nucleate and image the nanobubbles in the water film. All the observations were done at room temperature (R.T.: 22°C) and without flow in the liquid cell. Long durations localized TEM observation of the sample

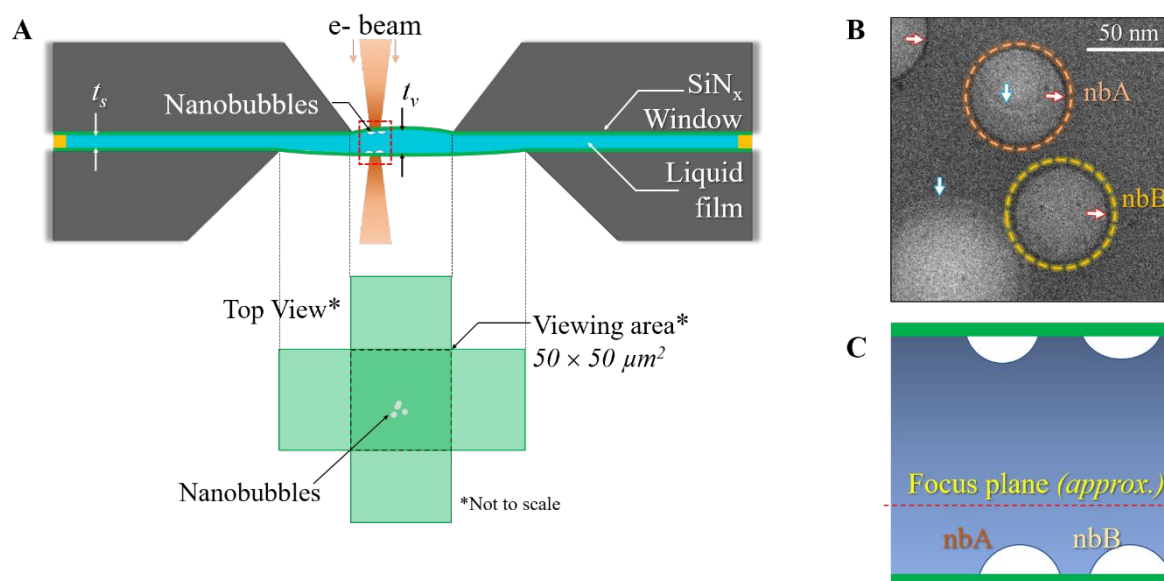


Figure 1 Nanobubble observation in a liquid cell. (A) Schematic of the liquid cell used to observe nanobubbles. Nanobubbles are nucleated heterogeneously at the water-SiN_x interface due to the e-beam induced radiolysis process. The E-chips are aligned in a crossed configuration, as represented in their top view. The SiN_x windows bow due to the high vacuum of the TEM column, resulting in massive thickness increase in the central region of the liquid cell, as depicted by t_s : spacer height (150 nm), and t_v : film thickness at viewing region (approx. hundreds of nm to few microns).⁷⁴ (B) TEM image showing the region of interest: nanobubbles A and B (in short: nbA and nbB). The initial distance between the three-phase contact lines of these nanobubbles is 20 nm. These surface nanobubbles are nucleated on the bottom SiN_x window. Few nanobubbles, present on the top SiN_x window, can also be seen in the TEM image. Red and blue bordered arrows are used to depict the bubbles at the bottom and top windows, respectively. (C) Side view representation of the TEM image in (B). The approximate focus plane during the imaging is also shown in the schematic.

was possible due to the thermionic emission source (LaB₆ filament). In our experiment, the typical beam current density measured at the CMOS camera sensor was 1.03 A/cm². All the images were acquired using a CMOS (Rio 16, Gatan Inc., U.S.A.) at 40 fps, 1K (1024×1024 pixels) resolution. In-house developed MATLAB code was used for the image preprocessing. Since the TEM images inherently have a low signal-to-noise ratio, the Gaussian filter was deployed to smoothen out the TEM images, and the Canny edge detection algorithm was used for detecting edges of the nanobubbles. The edge detected binary image was then fused on the original TEM image and the physical measurements were carried using an open-source scientific image analysis package: Fiji⁵⁶.

Results and Discussion

Experimental Observation

LPEM provides the opportunity to nucleate and directly observe nanobubbles and their interfacial phenomenon with high temporal and spatial resolution. In LPEM, the nucleation of nanobubbles can be accounted to the formation of gaseous molecules due to the electron-beam mediated radiolysis of water molecules and their successive agglomeration at the SiN_x surface (heterogeneous nucleation).⁵⁷ It is important to note that the heating effect of the electron beam on the liquid sample at the used beam parameters and consequently, the temperature increase is barely 2-3°C and can therefore be neglected.⁵⁸

Figure 1B shows the TEM image of the nanobubbles. The observed nanobubbles are in closer vicinity, thus providing the

opportunity to study the nanobubble's unique interplay. The contact angle of the nanobubbles could not be measured from the 2D images and was assumed to be below 90° from the gas side. This assumption agrees with previous studies which have clarified a definite distinction between the macroscopic and nanoscopic contact angles.^{5,32,37} Since the bubbles were nucleated in-situ, the radiolysis and the sequential events leading to the *status quo* had already begun and succeeded for some time, hence the experimental observation began at the time t_0 . The time-sequential information of these nanobubbles, before their coupled interplay, has been provided in the ESIT (Figure S2). The image frame (Figure 1B) also shows nanobubbles with bright boundaries, in contrast to darker boundaries of nbA and nbB. These boundaries are the Fresnel fringes which can be used to estimate the relative position of the bubbles.⁴⁹ The bubbles with the brighter fringes are on the upper SiN_x window, and due to their certain distance from the in-focus plane (Figure 1C), are not considered in this study. Additionally, the gap between the nanobubbles on the adjacent SiN_x windows is too large for the nanobubbles to have strong interactions between them. The only probable effect bubbles present on the upper window may have is the variations in the path length of electrons due to the changing bubble height, and hence, varying gas oversaturation in the liquid. However, even this effect was not persistent as we observed instances where no change in the size of nbA was observed as the bubble in the adjacent window shrinks. One such instance to show the negligible interaction between the bubbles present on the adjacent windows is given in the ESIT (Figure S3). Hence, the nanobubbles present on the adjacent SiN_x windows are assumed to be independent or weakly interacting in

comparison to the nanobubbles on the same window with much less gap between them. Moreover, since the prime focus of the present study was to understand the interplay between the neighboring nanobubbles, we chose the bubbles on the lower window having separation less than 20 nm.

Initially, at 0 s ($t = t_0 + 0$ s; same nomenclature else specified otherwise) the initial contact radii of the selected nanobubbles nbA and nbB, measured using $radii = \sqrt{area/\pi}$, was 31.5 nm and 27 nm, respectively. Both the nanobubbles were circular with very low deformity. As the e-beam irradiation continues, the nbA exhibits a gradual increase in its contact radius at 0.07 nm/s, whereas no increase in nbB's contact radius was observed. Consequently, the gap between the adjacent interfaces also reduced from 19.5 nm to 12 nm in the initial 100 s, owing to the monotonic growth in nbA's contact radius. The variation of the contact area and the distance between nanobubbles' contact lines for the initial 100 s is included in the ESI† (Figure S4).

Figure 2A-F shows the time sequence of the observed phenomenon. On irradiating the region of interest for around 95 s, the nbA, unexpectedly, begins to shrink as its contact area reduces from 4890 nm² to 2094 nm² in around 34 s, as shown in Figure 2G. Figure 2A-C demonstrates the shrinking of nbA. However, the nbB continues its trend of infinitesimal increase in the contact area. Further, the nbA regrows to the contact area 3870 nm² in 12 s. It is evident that the nanobubbles, nbA and nbB, behave distinctly, as nbA is a freely growing-shrinking nanobubble whereas nbB exhibits strong pinning in its contact line. The pulsating of nbA and its effect on the contact line of nbB can also be seen in Figure 2D-F. In our experimental study, nanobubbles were expected to grow due to oversaturation conditions under the continuous electron beam irradiation of the water.^{49,59} However, pulsations were observed for the nbA as shown in Figure 2G. Distinctively, the stability of nbB and its reluctance to exhibit similar dynamics can be accounted to the strong pinning of the contact line. The stability of the nanobubbles has, indeed, been attributed to the contact line pinning by several studies in the past.^{37,43,60} The pinning behavior of the contact line might be due to any possible chemical heterogeneities, which can be present on the smoothest of surfaces.⁵ In a similar context, a recent study has experimentally demonstrated the role of adsorbed gas layers on the surface, which exhibits solid-like rigidity, in limiting the mobility of micro-pancakes.⁶¹ The presence of such adsorbed layers is unlikely to be observed by a TEM, however, they might be responsible for the stability of nbB.

Anisotropic depinning in nanobubbles

The unpinned nbA undergoes series of grow-shrink undulation before stabilizing and following its usual growth pathway. Further, these undulations in nbA induced deformity in nbB, which tends to elongate the nbB. Figure 3A shows the variation of circularity of the studied nanobubbles. Here, circularity is defined as 4π times the ratio of area (A) to the square of the perimeter (P), i.e., $Circ. = 4\pi(A/P^2)$. The circularity value of 1 indicates a perfect circle, whereas any decline in its value

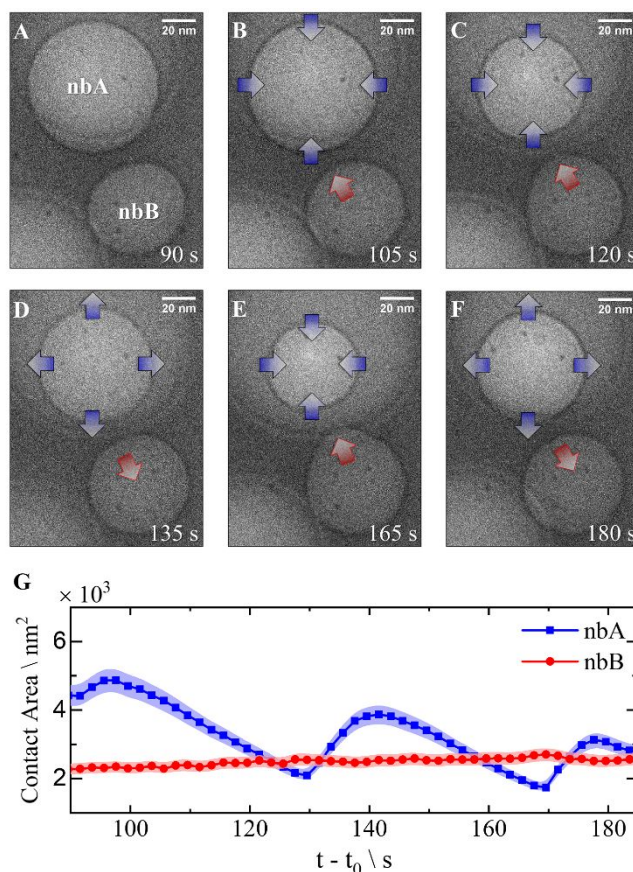


Figure 2 Time sequence images demonstrating the interfacial interplay between nanobubbles observed using TEM. (A) TEM image showing the state of nanobubbles at $t - t_0 = 90$ s. (B,C) The shrinking or leaking of nbA induces elongation in nbB, directed towards nbA. (D) The expansion or growth of nbA pushed the adjacent interface of nbB. (E,F) nbA and nbB demonstrating the pull-push phenomenon, induced due to the grow-shrink mechanism of nbA. Blue and Red arrows show the direction of the interface movement for nbA and nbB, respectively. (G) Temporal variation of nanobubble contact area for nbA and nbB. nbA exhibits growth-shrinkage behaviour, however, nbB remains mostly firm in its contact area. The TEM video of these bubbles is available in the ESI† (Movie M1).

indicates the extent of elongation. The reduced circularity of nbB demonstrates its deformation, whereas the circularity of nbA continues to be closer to 1. It was observed that while nbA continued to maintain its circular form due to its unpinned interface, nbB deformed asymmetrically. Moreover, the undulations in the nbA also lead to the variation in the distance between their three-phase contact lines, i.e., the gap varies between 12 nm to 18 nm (Figure 3B). We also measured the feret angle for nbB to understand the angularity and directionality of the deformation in nbB. Feret angle is the angle between the line segment joining two farthest points in an enclosed entity with the horizontal line. In Figure 3C, the feret angle was observed to fluctuate in two discrete ranges, (a) 15°-50°, and (b) 100°-135°. This demonstrates a strong association between the pulsation in nbA and deformation in nbB. For the shrinking phase of nbA, the feret angle remained between 100°-135°, thus confirming that nbB's interface is pulled directionally towards nbA due to its shrinking. Similarly, for the growing phase of nbA, the feret angle remained between 15°-50°, demonstrating push from the growing nbA's interface. The

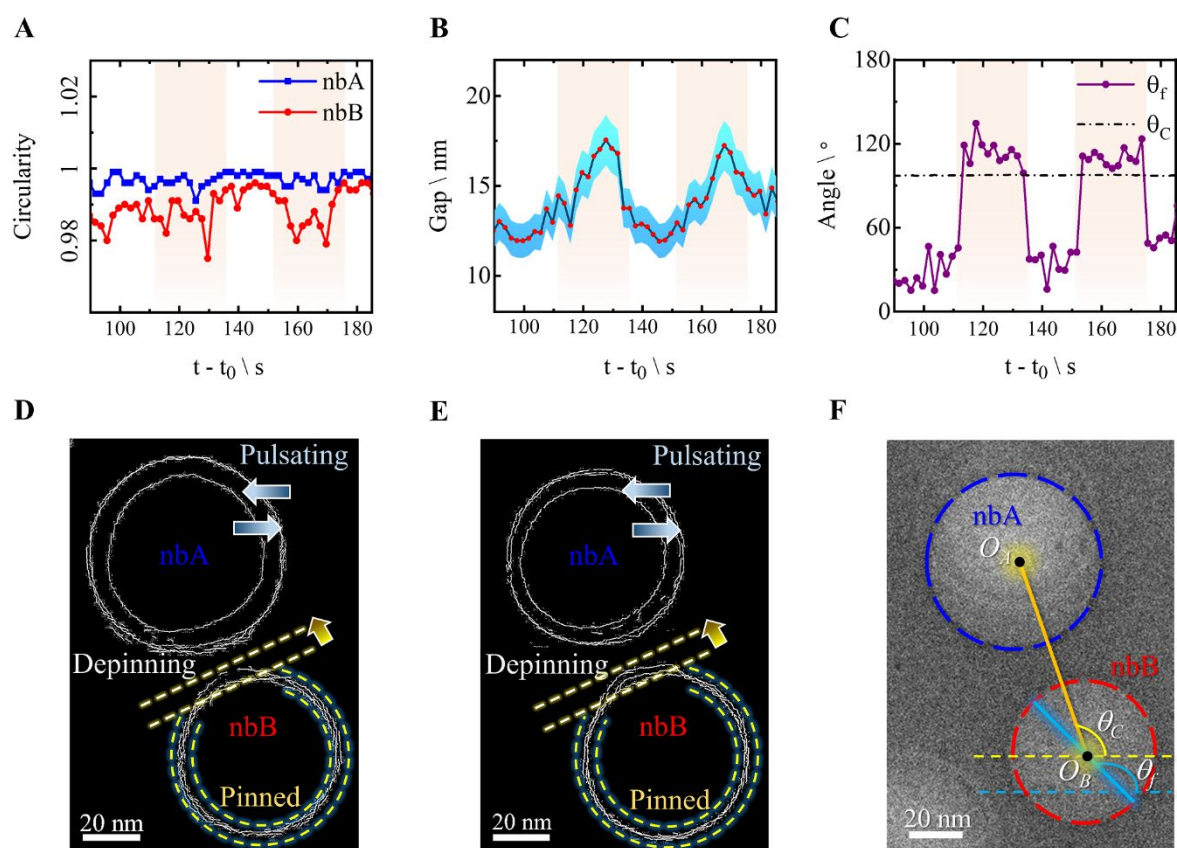


Figure 3 Anisotropic depinning of nanobubbles. (A) Temporal variation of circularity for nanobubble nbA and nbB. (B) Variation of the gap between the nanobubbles. (C) Feret angle and the angle formed by joining the centroids of nbA and nbB. The shaded region in (A), (B) and (C) highlights the directional deformation of the nbB induced due to nbA. (D) Contact line of the nanobubbles traced for the first shrink-grow observation at the time: 111 s, 125 s and 137 s. nbA shows the pulsating behaviour, while the nbB shows depinning along edge adjacent to nbA and pinning along the opposite edge. (E) Contact line of nanobubbles for second shrink-grow observation at time: 155 s, 165 s and 175 s. Similar anisotropic depinning is observed in nbB. (F) The reference image showing the measured parameters. O_A and O_B are the centroids of nbA and nbB, respectively. θ_f and θ_c are the feret angle and the centroid angle, respectively.

variation of feret angle, either parallel or perpendicular to the line joining the centroids of nanobubbles (Figure 3F) reassures the coupled behavior of the nanobubbles' interfaces. The measured parameters plotted in Figure 3B-C are shown in Figure 3F.

Further, the contact lines of these bubbles were traced using an edge detection algorithm to understand the deformation and the depinning of the nbB. Interestingly, it was observed that the contact region of the nbB, farther from the nbA, remained completely pinned to the surface during the whole phenomenon (Figure 3D-E). Figure 3D shows the contact boundary of the nanobubbles observed during the first shrink-grow cycle, i.e., at time 111 s, 125 s and 135 s. Pulsating of nbA and the consequent depinning of the adjacent interface of nbB, highlighted by blue and yellow arrows, respectively, can be seen in Figure 3D. A similar phenomenon of selective depinning was observed again at 154 s to 175 s into the observation, as shown in Figure 3E. Previously, the distortions in nanobubbles' pair were also observed by Park et. al, however, they observed it specifically in the larger nanobubble exhibiting growth due to the Ostwald ripening.⁴⁰ Moreover, they did not observe the asymmetrical depinning behavior in their experiments. In

addition, we also observed the pushing of nbB's interface when the nbA enters the growth regime.

For a better insight into the phenomenon, let us refocus on the reasons that contributed towards the pulsations in the nbA's contact line and successively led to the anisotropic depinning. Because of the continuous e-beam exposure, the gas oversaturation in the irradiated region accumulates and the nbA grows due to its unpinned three-phase contact line, which can be perceived from the TEM images. However, nbB is also expected to grow due to the increase in oversaturation, which cannot be perceived in the 2-D TEM images due to its pinned three-phase contact line. In an analytical study, Lohse and Zhang suggested that for a pinned nanobubble, the equilibrium radius varies inversely with the oversaturation, ($R_e = L_c/2\zeta$, where R_e is the equilibrium radius, L_c is the contact length, and ζ is the gas oversaturation), hence an increase in the oversaturation will compel the nanobubble to swell, thus increasing in its height and effective volume.⁴³ The probable side views of the nanobubbles and the observed phenomenon is shown in Figure 4A, where, any increase in the size of nbA is accompanied by an increase in height of nbB, and vice versa. The observed anisotropic depinning coupled with the shrinking of the nbA can be explained as follows (Figure 4B): the

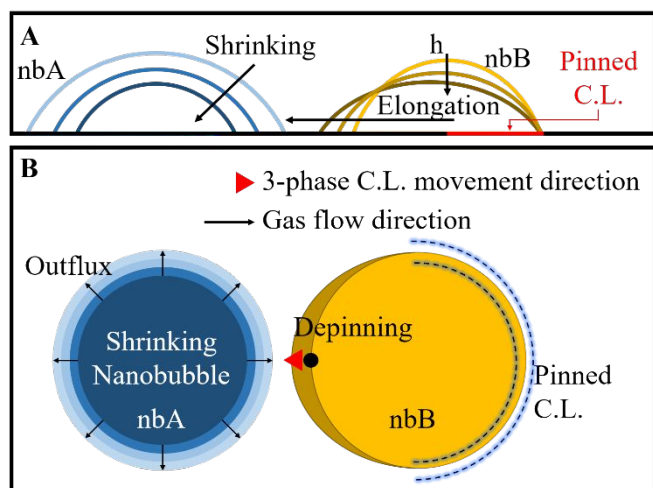


Figure 4 (A) Schematic of the probable side view of the nanobubbles shows the shrinking of the nbA initiates the anisotropic depinning of nbB's three-phase contact line. (B) Role of increase in localized gas concentration in the anisotropic depinning of surface nanobubbles. The lighter blue region around the nbA shows the level of high gas concentration.

simultaneous shrinking of nbA and nbB leads to gas outflux in their peripheral region. The gas concentration is expected to be higher in the region between the nanobubbles near the solid interface, due to the damped diffusion of gas molecules near the interfaces.^{31,62} As the contact line of nbA is moving away, these gas molecules then transmit to the pinned nbB, resulting in the growth of its partial portion. Nanobubbles are in dynamic equilibrium with the gas molecule in the liquid and the gas outflux is balanced by the influx through nanobubbles' interfaces.⁶³ This, in general, does not affect depinning. However, asymmetric distribution of gas oversaturation around a pinned nanobubble leads to anisotropic depinning of its three-phase contact line. Interestingly, the pinning force at the interface for the remaining region was observed to be strong enough to keep the surface pinned without compensating for surface tension. In addition, the interface farther from the region between the nanobubbles does not experience any dramatic changes in the relative gas saturation, and hence, the remaining three-phase contact line of the nanobubble remains pinned, as shown by the red color in Figure 4A. The schematic in Figure 4B also weighs the factors responsible for the observed anisotropic depinning, where the increased local oversaturation around the pulsating nanobubble is responsible for selective depinning of a strongly pinned nanobubble.

Moreover, the relative positioning of these nanobubbles also promotes the pulsating effect in the nanobubbles. As the nbA expands towards nbB and the distance between the nanobubbles' three-phase contact line reduces, the presence of nbB and the thin film formed between the nanobubbles hinders the further expansion of nbA. The stability of thin-film and the nbA's intrusion into the thin film not only suppresses the growth of the nbA, but also leads to repulsions between the two nanobubbles due to their interacting double layers. The cumulative effect of strong interfacial repulsions and the presence of pinned nanobubble triggers the shrinking of nbA. The outflux from the nbA creates oversaturation in the vicinal

liquid, thus leading to the anisotropic depinning of the pinned nanobubble. The outflux from nbA and the successively increased oversaturation in the liquid further halts the shrinking of nbA and leads to the growth in the size of nbA. The overshoot in the radius of curvatures due to the inertia in interfaces' motion creates a pulsating effect in the size of nanobubbles. While the pulsations in the nbA are observed due to the increase in its lateral size (as shown in Figure 2G), such variations in nbB are impossible to observe using TEM.

Similar phenomenon was observed on multiple occasions while observing other nanobubble pairs, however, the presence of more nanobubbles at relative adjacency seems to impact the time scales and bubble pulsations in the phenomenon. The time sequence imagery and brief description of such events have been provided in the ESI† (Figure S5, S6, and S7), where deformation in the three-phase contact line of the nanobubbles could be observed due to the shrinkage or growth of adjacent nanobubble. On observing a nanobubble pair at a lower electron beam intensity, we found the anisotropic depinning to be lower in magnitude due to the lower relative oversaturation at a low electron dose environment, as shown in the ESI† (Figure S5). This reassures the role of localized oversaturation on the anisotropic depinning of pinned surface nanobubbles. However, the pushing of nbB's three-phase contact line due to the pulsating nbA needs to be discussed further while considering the nanoscale forces at play.

The thin film between the nanobubbles, with varying thickness of 6-20 nm, was observed to be stable experimentally. Moreover, the nanobubbles interact across this thin film, which causes the pull-push phenomenon between the nanobubble's interfaces. Nanobubbles' surface, or in general all gas-water interfaces, is charged negatively due to the strong adsorption of hydroxide ions,^{64,65} which prompts an electric force field around their interfaces. This electric field influences the ion distribution around a nanobubble, which leads to the generation of diffused electric double layer (EDL) around its interface.⁵⁰ The double layers of two individual nanobubbles in the vicinity lead to the interactions between their interfaces due to the accumulation of counterions at the peripheral region. Due to the likeness of the interfacial charges, the double-layer interaction is repulsive in nature. In addition, the van der Waals interactions are accounted for the attractive behavior and are dominant as the distance between the bubbles reduces. Hence, cumulatively, the nanobubble pair exhibits attractive-repulsive behavior along with their interfaces, which is a factor of the separation distance between the nanobubbles, size of the bubbles, surface charge, and the physical properties of the nucleating medium. These interactions are analogous to the colloidal particles interacting in the bulk medium,⁶⁶ except that the nanobubbles are also coupled via the gas exchanges (mass diffusion) between them. Further, the hemispherical shape of the bubbles, along with their soft interfaces and interfacial pinning further increases the complexity in the quantifiable modeling of such phenomenon, however, the nature of interactions can be discussed qualitatively. The Debye-Hückel constant, which is proportional to the ionic concentration of the liquid, plays a critical role in determining the interactive behavior between the

nanobubbles. It is important to note here that even though no salt was added in this study, the ionic concentration in the water is affected by the electron beam dose rate. For the lower electron dose rates, the pH of the water remains unaffected, but at higher electron dose rate values, the pH of the water reduces significantly,⁵⁸ implying an increase in the ionic concentration of the H_3O^+ ions. For the typical TEM dose (10^8 Gy/s), the pH of the water is expected to lie between pH 4-5.⁵⁸ The increased H_3O^+ concentration, hence the thin double layer, maybe the reason for pull-push behavior between the nanobubble interfaces, which can be justified by the feret angle variation between 15° - 50° and 100° - 135° in Figure 3C. In case of the pH value closer to the neutral cases (pH \sim 7), the double layer would be much thicker, and the interaction is expected to be repulsion dominant. Moreover, the nature of gas molecules dissolved in the water is highly unlikely to affect the charge at the interface, except for CO_2 . Most of the gases dissolved in water, such as N_2 , O_2 , He, Ar, CH_4 , H_2 , etc are non-polar and inert in nature and have no impact on the pH of water.⁶⁷ However, CO_2 is arguably known to reduce the pH of the water and impart negative charge to the water-gas interface.⁶⁸ Hence, the concentration of CO_2 in water will in fact affect the charge concentration, Debye-Hückel constant, and the strength of EDL, which may impact the pull-push phenomenon.

Weakened repulsions and coalescence

In our experiment, we observed the coalescence of nanobubbles after nearly 18 minutes from the beginning of the observation (t_0). During the observation, the nanobubble pair underwent multiple pull-push and anisotropic depinning events, details of which are provided in the ESI† (Figure S8). It is important to note here that the bubbles have existed for a longer time as they were already nucleated when the observation was initiated. Recollecting the derogatory electron beam conditions and the fluctuation in gas saturation conditions caused by them, our observation reassured the long-term existence of nanobubbles and their metastability. In the due course, we observed the coalescence of the nanobubbles. The snapshots of nbA and nbB before and during merging are shown in Figure 5A-D. As discussed in the previous section about the EDL, the bubbles should demonstrate hesitance to merging, due to the attractive repulsive equilibrium at a lower separation gap (Figure 5). That was, indeed, the reason for the observed longevity of nanobubbles. However, the phenomenon exhibited by nanobubbles is intricate and depends on the various physio-chemical phenomenon, which may be transient and changes as the experimental parameters change. Although the formation of EDL hinders the coalescence initially, the continuous exposure of the sample to the electron beam and the accumulative buildup of gas saturation may be the reason behind the observed coalescence. A previous study on the effect of gas concentration in liquid on the bubble coalescence also points towards the increased coalescence.⁶⁹ The accumulation of gas molecules and their steric effects might be responsible for the displacement of ions from the interfacial region of nanobubbles. This is further supported by the higher

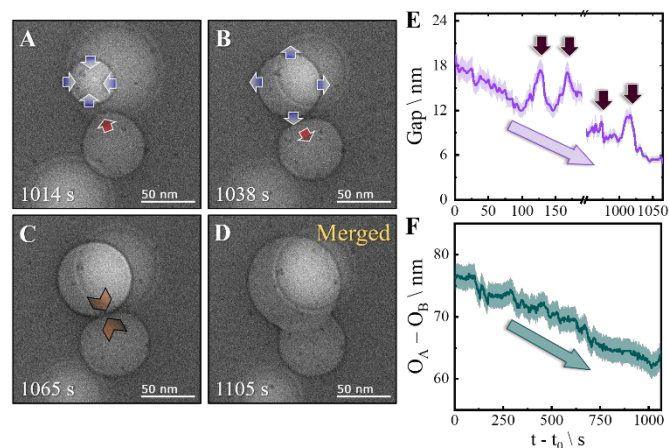


Figure 5 Time sequence snapshots of nbA and nbB for the time (A) 1014 s; (B) 1038 s; (C) 1065 s and (D) 1105 s. The blue and red arrows in (A) and (B) show the direction of the interface movement in nbA and nbB, respectively, whereas the orange arrow in (C) shows the initiation of merging. The bubble merged after 18 minutes of observation. The shape of the bubble after merging verifies that the observed bubbles are surface nanobubbles. (E) Variation of gap between the nanobubbles for time 0 s – 180 s (initial observation) and 950 s – 1065 s (before merging). The black arrow shows the increased gap due to the shrinking of nbA. The reduced repulsions between the interfaces have led to a decrease in the overall gap between the bubbles. (F) Variation of center-to-center distance between the nanobubbles for the complete 18 minutes of observation. The reduced repulsions between the nanobubbles due to the accumulative oversaturation increase are evident as the center-to-center distance decreases monotonically for the whole observation.

steady-state concentration of hydrogen molecules in the radiolysis of water,⁵⁸ and the high diffusion coefficient of H_3O^+ ion.^{70,71} The resultant may be a weaker EDL and reduced repulsive force between the nanobubbles. Additionally, few previous studies also suggested that the gas molecules' number density is generally higher near the liquid-solid interfaces, owing to strong gas-solid interactions.^{72,73} This is further favored by the inherently higher number of molecules between the neighboring bubbles' diffused interfaces.^{35,40} The increased gas saturation may play a vital role in suppressing the repulsive behavior, which leads to the merging of the nanobubbles. Interestingly, the gap between the nanobubbles' three-phase contact line (as shown in Figure 5E), which in the earlier stage of interactions fluctuated in the range of 12-20 nm, also reduced to 5-10 nm range before merging, which is another indication of the reduced magnitude of repulsive behavior. The decreased repulsive behavior as a function of irradiation time is also evident from the reduced center to center distance between the nanobubbles, as shown in Figure 5F. The nbA was observed to move towards the pinned nbB while pulsating as their center-to-center distance reduced from 77 nm to 64 nm while the whole observation was carried.

Conclusions

Using liquid-phase electron microscopy technique, this work provides insight into the nanobubble dynamics and interactions with high spatial and temporal resolutions. Previously, the counterintuitive longevity of surface nanobubbles has been long attributed to the contact line pinning, however, this study

contributes towards expanding the existing knowledge by experimentally demonstrating the existence of surface nanobubbles with and without contact line pinning. In addition, our work also captures the anisotropic depinning of the pinned nanobubbles and reveals the role of localized gas oversaturation in this asymmetric interfacial phenomenon. The pulsations in the unpinned nanobubble create an environment with fluctuating gas concentration and are responsible for the anisotropic depinning. Further, this study highlights the effect of the ionic concentration on the coupling of the nanobubbles' interfaces and the pull-push behavior, which is attributed to the EDLs encompassing the nanobubbles and their successive interactions. The present study also reveals the role of accumulative gas saturation in suppressing the EDL's repulsive interaction, which reduces the nanobubbles' reluctance to merge. These findings not only provide insight into the dynamic nanobubble behavior but also explains the importance of EDL in rendering the longevity to nanobubbles, which in some cases have been few days. This work also illustrates the capability of the LPEM technique in studying the nanobubbles' dynamics, which so far, has mostly been examined through the MD simulation lens. The focus in future studies will be on controlling the gas oversaturation and ionic concentration in the liquid by improvising the experimental methods so that the influence of these parameters can be quantified for in-depth understanding.

Author Contributions

The manuscript was finished with the contributions of all authors. All authors have given their approval for the final version of the manuscript.

Conflicts of interest

There are no conflicts to declare.

Acknowledgements

The authors would like to thank Yuzen Masame and Ryota Kimura from the Aerospace Applied Physics Laboratory, Kyushu University for droplet contact angle measurements. This research was partially funded by the Core Research for Evolutional Science and Technology project of the Japan Science and Technology Agency (JST-CREST) grant number JPMJCR18I1. S.N. acknowledges financial support from the Japanese Society for the Promotion of Science (JSPS) KAKENHI grant number JP20J13061. Y.T. acknowledges financial support from the Japanese Society for the Promotion of Science (JSPS) KAKENHI grant number JP19K23490.

Notes and references

- 1 P. Ball, *Nature*, 2003, **423**, 25–26.
- 2 S. Singh, J. Houston, F. Van Swol and C. J. Brinker, *Nature*, 2006, **442**, 526.
- 3 J. W. G. Tyrrell and P. Attard, *Phys. Rev. Lett.*, 2001, **87**, 176104.
- 4 P. Attard, M. P. Moody and J. W. G. Tyrrell, *Phys. A Stat. Mech. its Appl.*, 2002, **314**, 696–705.
- 5 D. Lohse and X. Zhang, *Rev. Mod. Phys.*, 2015, **87**, 981.
- 6 X. Zhang and D. Lohse, *Biomicrofluidics*, 2014, **8**, 1505.
- 7 J. L. Parker, P. M. Claesson and P. Attard, *J. Phys. Chem.*, 1994, **98**, 8468–8480.
- 8 H. Liu and G. Cao, *Sci. Rep.*, 2016, **6**, 1–10.
- 9 P. S. Epstein and M. S. Plesset, *J. Chem. Phys.*, 1950, **18**, 1505–1509.
- 10 S. Ljunggren and J. C. Eriksson, *Colloids Surfaces A Physicochem. Eng. Asp.*, 1997, **129–130**, 151–155.
- 11 V. S. J. Craig, *Soft Matter*, 2011, **7**, 40–48.
- 12 X. H. Zhang, A. Quinn and W. A. Ducker, *Langmuir*, 2008, **24**, 4756–4764.
- 13 A. J. Jadhav and M. Barigou, *Langmuir*, 2020, **36**, 1699–1708.
- 14 X. Su, J. Wu and B. J. Hinds, *Adv. Mater. Interfaces*, 2015, **2**, 1500102.
- 15 Z. H. Wu, H. B. Chen, Y. M. Dong, H. L. Mao, J. L. Sun, S. F. Chen, V. S. J. Craig and J. Hu, *J. Colloid Interface Sci.*, 2008, **328**, 10–14.
- 16 T. Temesgen, T. T. Bui, M. Han, T. il Kim and H. Park, *Adv. Colloid Interface Sci.*, 2017, **246**, 40–51.
- 17 X. Hu, X. Gong, M. Zhang, H. Lu, Z. Xue, Y. Mei, P. K. Chu, Z. An and Z. Di, *Small*, 2020, **16**, 1907170.
- 18 J. Zou, H. Zhang, Z. Guo, Y. Liu, J. Wei, Y. Huang and X. Zhang, *Langmuir*, 2018, **34**, 14096–14101.
- 19 Y. Lu, *Tribol. Int.*, 2019, **137**, 267–273.
- 20 C. K. Fang, H. C. Ko, C. W. Yang, Y. H. Lu and I. S. Hwang, *Sci. Rep.*, 2016, **6**, 1–10.
- 21 H. Teshima, K. Takahashi, Y. Takata and T. Nishiyama, *J. Appl. Phys.*, 2018, **123**, 054303.
- 22 S.-T. Lou, Z.-Q. Ouyang, Y. Zhang, X.-J. Li, J. Hu, M.-Q. Li and F.-J. Yang, *J. Vac. Sci. Technol. B Microelectron. Nanom. Struct.*, 2000, **18**, 2573.
- 23 H. An, B. H. Tan, Q. Zeng and C. D. Ohl, *Langmuir*, 2016, **32**, 11212–11220.
- 24 N. Hain, S. Handschuh-Wang, D. Wesner, S. I. Druzhinin and H. Schönherr, *J. Colloid Interface Sci.*, 2019, **547**, 162–170.
- 25 B. Bhushan, Y. Pan and S. Daniels, *J. Colloid Interface Sci.*, 2013, **392**, 105–116.
- 26 C. U. Chan and C. D. Ohl, *Phys. Rev. Lett.*, 2012, **109**, 174501.
- 27 B. P. Dyett and X. Zhang, *ACS Nano*, 2020, **14**, 10944–10953.
- 28 B. H. Tan, H. An and C. D. Ohl, *Phys. Rev. Lett.*, 2017, **118**, 054501.
- 29 L. Zhang, B. Zhao, L. Xue, Z. Guo, Y. Dong, H. Fang, R. Tai and J. Hu, *J. Synchrotron Radiat.*, 2013, **20**, 413–418.
- 30 L. Zhou, X. Wang, H. J. Shin, J. Wang, R. Tai, X. Zhang, H. Fang, W. Xiao, L. Wang, C. Wang, X. Gao, J. Hu and L. Zhang, *J. Am. Chem. Soc.*, 2020, **142**, 5583–5593.
- 31 S. Hirokawa, H. Teshima, P. Solís-Fernández, H. Ago, Y. Tomo, Q. Y. Li and K. Takahashi, *ACS Omega*, 2020, **5**, 11180–11185.
- 32 T. W. Huang, S. Y. Liu, Y. J. Chuang, H. Y. Hsieh, C. Y. Tsai, W. J. Wu, C. T. Tsai, U. Mirsaidov, P. Matsudaira, C. S. Chang, F. G. Tseng and F. R. Chen, *Soft Matter*, 2013, **9**, 8856–8861.

- 33 Y. Tomo, Q. Y. Li, T. Ikuta, Y. Takata and K. Takahashi, *J. Phys. Chem. C*, 2018, **122**, 28712–28716.
- 34 E. R. White, M. Mecklenburg, S. B. Singer, S. Aloni and B. C. Regan, *Appl. Phys. Express*, 2011, **4**, 055201.
- 35 S. Nag, Y. Tomo, K. Takahashi and M. Kohno, *Langmuir*, 2021, **37**, 874–881.
- 36 X. H. Zhang, X. Zhang, J. Sun, Z. Zhang, G. Li, H. Fang, X. Xiao, X. Zeng and J. Hu, *Langmuir*, 2007, **23**, 1778–1783.
- 37 H. Teshima, T. Nishiyama and K. Takahashi, *J. Chem. Phys.*, 2017, **146**, 014708.
- 38 N. De Jonge and F. M. Ross, *Nat. Nanotechnol.*, 2011, **6**, 695–704.
- 39 D. Shin, J. B. Park, Y. J. Kim, S. J. Kim, J. H. Kang, B. Lee, S. P. Cho, B. H. Hong and K. S. Novoselov, *Nat. Commun.*, 2015, **6**, 1–6.
- 40 J. B. Park, D. Shin, S. Kang, S. P. Cho and B. H. Hong, *Langmuir*, 2016, **32**, 11303–11308.
- 41 M. Tortora, S. Meloni, B. H. Tan, A. Giacomello, C. D. Ohl and C. M. Casciola, *Nanoscale*, 2020, **12**, 22698–22709.
- 42 B. H. Tan, H. An and C. D. Ohl, *Phys. Rev. Lett.*, 2018, **120**, 164502.
- 43 D. Lohse and X. Zhang, *Phys. Rev. E - Stat. Nonlinear, Soft Matter Phys.*, 2015, **91**, 031003.
- 44 B. H. Tan, H. An and C. D. Ohl, *Phys. Rev. Lett.*, 2019, **122**, 134502.
- 45 Z. Guo, Y. Liu, Q. Xiao and X. Zhang, *Langmuir*, 2016, **32**, 11328–11334.
- 46 J. Qian, V. S. J. Craig and M. Jehannin, *Langmuir*, 2019, **35**, 718–728.
- 47 Z. Guo, X. Wang and X. Zhang, *Langmuir*, , DOI:10.1021/acs.langmuir.9b00772.
- 48 D. S. Bull, N. Nelson, D. Konetski, C. N. Bowman, D. K. Schwartz and A. P. Goodwin, *J. Phys. Chem. Lett.*, 2018, **9**, 4239–4244.
- 49 Y. Tomo, K. Takahashi, T. Nishiyama, T. Ikuta and Y. Takata, *Int. J. Heat Mass Transf.*, 2017, **108**, 1460–1465.
- 50 J. N. Meegoda, S. A. Hewage and J. H. Batagoda, *Langmuir*, 2019, **35**, 12100–12112.
- 51 B. H. Tan, H. An and C. D. Ohl, *Phys. Rev. Lett.*, 2020, **124**, 134503.
- 52 N. Nirmalkar, A. W. Pacek and M. Barigou, *Soft Matter*, 2018, **14**, 9643–9656.
- 53 A. Carambassis, L. C. Jonker, P. Attard and M. W. Rutland, *Phys. Rev. Lett.*, 1998, **80**, 5357–5360.
- 54 N. F. Bunkin, A. V. Shkirin, N. V. Suyazov, V. A. Babenko, A. A. Sychev, N. V. Penkov, K. N. Belosludtsev and S. V. Gudkov, *J. Phys. Chem. B*, 2016, **120**, 1291–1303.
- 55 J. N. Israelachvili, *Intermolecular and Surface Forces*, Elsevier Inc., 3rd editio., 2011.
- 56 J. Schindelin, I. Arganda-Carreras, E. Frise, V. Kaynig, M. Longair, T. Pietzsch, S. Preibisch, C. Rueden, S. Saalfeld, B. Schmid, J. Y. Tinevez, D. J. White, V. Hartenstein, K. Eliceiri, P. Tomancak and A. Cardona, *Nat. Methods*, 2012, **9**, 676–682.
- 57 J. M. Grogan, N. M. Schneider, F. M. Ross and H. H. Bau, *Nano Lett.*, 2014, **14**, 359–364.
- 58 N. M. Schneider, M. M. Norton, B. J. Mendel, J. M. Grogan, F. M. Ross and H. H. Bau, *J. Phys. Chem. C*, 2014, **118**, 22373–22382.
- 59 Qh. Kim, D. Shin, J. Park, D. A. Weitz and W. Jhe, *Appl. Nanosci. 2018 111*, 2018, **11**, 1–7.
- 60 Y. Liu and X. Zhang, *J. Chem. Phys.*, 2014, **141**, 134702.
- 61 H. Teshima, Y. Takata and K. Takahashi, *Appl. Phys. Lett.*, 2019, **115**, 071603.
- 62 J. Lu, Z. Aabdin, N. D. Loh, D. Bhattacharya and U. Mirsaidov, *Nano Lett.*, 2014, **14**, 2111–2115.
- 63 M. P. Brenner and D. Lohse, *Phys. Rev. Lett.*, 2008, **101**, 214505.
- 64 J. K. Beattie, A. M. Djerdjev and G. G. Warr, *Faraday Discuss.*, 2008, **141**, 31–39.
- 65 M. Takahashi, K. Chiba and P. Li, *J. Phys. Chem. B*, 2007, **111**, 1343–1347.
- 66 H. Reerink and J. T. G. Overbeek, *Discuss. Faraday Soc.*, 1954, **18**, 74–84.
- 67 G. Fricke, R. Carpenter and R. Battino, *J. Phys. Chem.*, 1973, **77**, 826–828.
- 68 M. Kowacz and G. H. Pollack, *J. Phys. Chem. B*, 2019, **123**, 11003–11013.
- 69 A. Brotchie, T. Statham, M. Zhou, L. Dharmarathne, F. Grieser and M. Ashokkumar, *Langmuir*, 2010, **26**, 12690–12695.
- 70 D. R. Lide and H. V. Kehiaian, *CRC Handb. Thermophys. Thermochem. DATA*, CRC Press, 2020.
- 71 J. Buffle, Z. Zhang and K. Startchev, *Environ. Sci. Technol.*, 2007, **41**, 7609–7620.
- 72 Y. H. Lu, C. W. Yang, C. K. Fang, H. C. Ko and I. S. Hwang, *Sci. Rep.*, 2014, **4**, 1–8.
- 73 S. Maheshwari, M. Van Der Hoef, J. Rodríguez Rodríguez and D. Lohse, *ACS Nano*, 2018, **12**, 2603–2609.
- 74 H. Wu, H. Su, R. R. M. Joosten, A. D. A. Keizer, L. S. van Hazendonk, M. J. M. Wirix, J. P. Patterson, J. Laven, G. de With and H. Friedrich, *Small Methods*, 2021, **5**, 2001287.